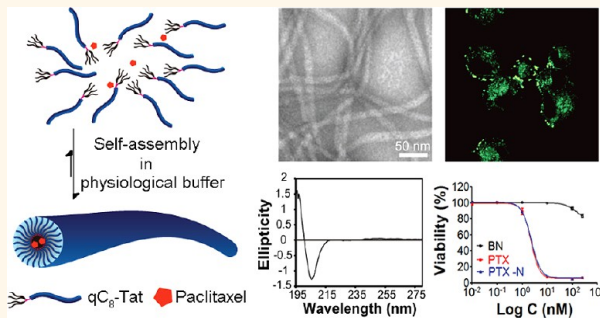


# Self-Assembled Tat Nanofibers as Effective Drug Carrier and Transporter

Pengcheng Zhang, Andrew G. Cheetham, Yi-an Lin, and Honggang Cui\*

Department of Chemical and Biomolecular Engineering, and Institute for NanoBioTechnology, The Johns Hopkins University, Baltimore, Maryland 21218, United States

**ABSTRACT** Cell penetrating peptides (CPPs) have been extensively explored as molecular vectors through covalent linkage to anticancer drugs to improve the drug's water solubility and to help overcome multidrug resistance. We report here the use of the Tat CPP as a molecular building unit to construct well-defined supramolecular nanofibers that can be utilized as a nanoscale vector to encapsulate the hydrophobic drug paclitaxel (PTX) (loading efficiency:  $89.7 \pm 5.0\%$ ) with a high loading capacity ( $6.8 \pm 0.4\%$ ). Notably, our TEM imaging results reveal that nanofibers containing a higher PTX content tend to be more flexible than those with a lower PTX content. Fluorescence and confocal microscopy imaging show that the Tat nanofibers can effectively transport encapsulated molecules into the cells through an adsorptive-mediated endocytosis pathway. Cytotoxicity experiments and flow cytometry measurements demonstrate that PTX loaded in the nanofibers exerts its cytotoxicity against cancer cells by arresting the cells at the G2/M phase, the same working mechanism as free PTX.



**KEYWORDS:** cell penetrating peptides · self-assembly · supramolecular nanostructures · paclitaxel · drug delivery

Cell penetrating peptides (CPPs) are a class of small cationic peptides (typically less than 20 amino acids) rich in lysines and/or arginines<sup>1,2</sup> and have attracted much attention within the drug delivery community due to their ability to transport cargos across cell membranes.<sup>3,4</sup> In most cases, CPP-assisted cargo transport is achieved by chemical conjugation of the cargo to a CPP through a degradable linker that allows for later release of the cargo within the cells.<sup>3,4</sup> For example, the HIV-derived Tat peptide has been conjugated to a wide range of cargos to improve their membrane penetration, including small molecular drugs,<sup>5</sup> peptides,<sup>6</sup> proteins,<sup>7</sup> oligonucleic acids,<sup>8</sup> and nanoparticles.<sup>9–11</sup> In sharp contrast to this conjugation strategy, the use of the Tat peptide and other CPPs as building blocks to create supramolecular nanostructures as nanoscale vectors has been relatively unexplored.<sup>12–14</sup> Here we report the use of the Tat<sub>48–60</sub> peptide as a molecular building unit to construct high-aspect-ratio nanofibers and the evaluation of the resultant CPP nanofibers as effective nanoscale transporters to deliver paclitaxel, a hydrophobic anticancer drug, into cancer cells.

Nanostructures of a high aspect ratio have been shown to interact with cells in

ways different from their spherical counterparts and could possess advantageous properties as drug carriers.<sup>15</sup> Previous reports have demonstrated that high-aspect-ratio structures have a prolonged blood circulation time,<sup>16</sup> broader biodistribution,<sup>17</sup> increased targeting efficiency,<sup>18</sup> altered cellular uptake,<sup>19</sup> and even different intracellular deposition.<sup>20</sup> From the perspective of molecular design, there are generally two self-assembly strategies to access high-aspect-ratio nanostructures. The first strategy is to form cylindrical micelles stabilized by a spontaneous curvature.<sup>21</sup> With the proper molecular design and under the appropriate conditions, small molecular or macromolecular amphiphiles could pack into a preferred cylindrical geometry as a result of balancing the effective volume of the hydrophilic head groups with that of the hydrophobic segments.<sup>22</sup> The end-capping energy associated with the two hemispherical end-caps placed at the ends of the cylindrical micelles drives the elongation of the assembled nanostructures.<sup>23</sup> The hydrophobic cores of the resultant micelles are suitable for encapsulation of hydrophobic drugs such as paclitaxel.<sup>24</sup> However, the strategy requires that the ratio of hydrophobic

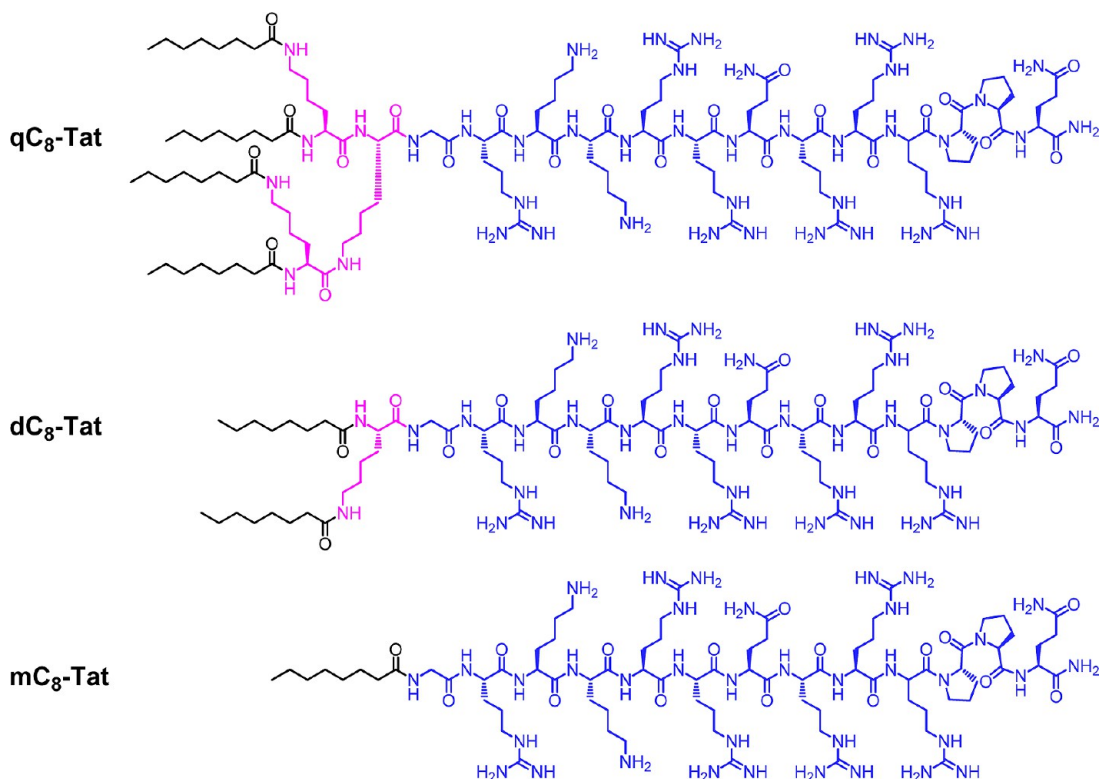
\* Address correspondence to  
hcui6@jhu.edu.

Received for review April 4, 2013  
and accepted June 11, 2013.

Published online June 11, 2013  
10.1021/nn401667z

© 2013 American Chemical Society

Chart 1. Structure of the three synthesized Tat peptide conjugates with differing numbers of octanoic acid tails (qC<sub>8</sub>-Tat, dC<sub>8</sub>-Tat, and mC<sub>8</sub>-Tat).



block to hydrophilic block be tailored within a precise range for formation of cylindrical micelles, which can often be challenging from the perspectives of both polymer synthesis and assembly.<sup>21,22</sup>

The second molecular design strategy is the use of molecular segments capable of forming directional, strong, attractive interactions, such as  $\pi$ – $\pi$  stacking, metal–ligand complexation, and hydrogen bonding.<sup>25</sup> One-dimensionality of the assembled morphology is a natural outcome of the directional interactions involved, although the morphology itself can vary, potentially giving rise to twisted ribbons,<sup>26</sup> nanotubes,<sup>27</sup> nanobelts,<sup>28</sup> or filaments.<sup>29–31</sup> In the context of biomedical applications, peptide-based building units are of particular interest due to their inherent biodegradability and tunable biocompatibility.<sup>32</sup> A significant majority of the work in this area has been focused on peptides or peptide derivatives containing  $\beta$ -sheet-forming sequences,<sup>31–35</sup> although  $\alpha$ -helical<sup>36</sup> and collagen mimetic<sup>37</sup> peptides have also been reported to self-assemble into nanofibers. In particular, Stupp and co-workers have designed a special class of peptide amphiphiles by incorporating a hydrocarbon tail onto a  $\beta$ -sheet-forming peptide that can self-assemble into high-aspect-ratio cylindrical nanofibers under physiological conditions.<sup>32,33,38,39</sup> The hydrophobic compartment within the peptidic nanofibers developed by Stupp<sup>40</sup> and others<sup>14,31,41,42</sup> enables the possibility for the sequestration of hydrophobic anticancer drugs.

However, the drug loading capacity (DLC) of these peptidic nanofibers is very low (less than 2%),<sup>14,40</sup> possibly due to either the limited domain size of the hydrophobic segment or the high degree of packing order among the hydrocarbons.<sup>14,43</sup>

We report here that the bioactive Tat peptide, when conjugated to hydrocarbon tails, can adopt a  $\beta$ -sheet secondary structure, thus leading to formation of 1D nanostructures. We synthesized three Tat conjugates with differing numbers of octanoic acid (C<sub>8</sub>) tails, namely, qC<sub>8</sub>-Tat, dC<sub>8</sub>-Tat, and mC<sub>8</sub>-Tat (Chart 1). Our design rationale is that by having multiple *short* hydrophobic tails the hydrophobic domain formed would be enlarged and less crystalline, thereby leading to a possible high DLC (Figure 1a). We chose the hydrophobic drug paclitaxel (PTX) as the model drug because of its approved use for treatments of breast cancer, ovarian cancer, and other cancer types.<sup>44,45</sup> Given its poor water solubility, PTX is often administered *via* nanoscale delivery vehicles. The DLC of PTX in these nanocarriers reported thus far rarely exceeds 5%.<sup>10,46–49</sup> Only in some particular cases was a high DLC reported,<sup>50–54</sup> often involving specific polymer design such as the use of hydrophobic aromatic side groups that are expected to have high affinity with PTX<sup>50–52</sup> or high energy input to obtain and stabilize PTX nanocrystals.<sup>53,54</sup> In this paper, the drug-loaded nanomedicine was prepared by directly dissolving in aqueous buffer a drug and conjugate mixture that was

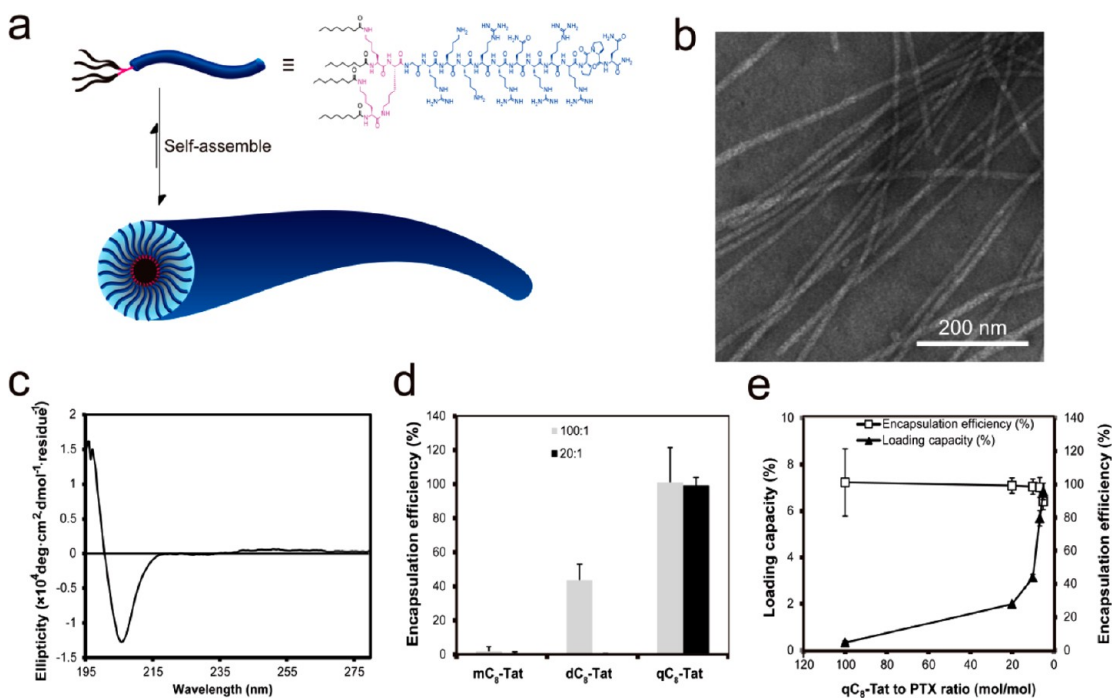


**Figure 1.** Self-assembly characterization and drug encapsulation studies of qC<sub>8</sub>-Tat. (a) Schematic illustration of the self-assembly of qC<sub>8</sub>-Tat into nanofibers. (b) TEM image of nanofiber formed by qC<sub>8</sub>-Tat in Dulbecco's phosphate-buffered saline (DPBS) at 2 mM. (c) Normalized CD spectrum of 400  $\mu$ M qC<sub>8</sub>-Tat nanofiber in DPBS. (d) Comparison of the PTX encapsulation efficiency for each Tat conjugate (mC<sub>8</sub>-Tat, dC<sub>8</sub>-Tat, and qC<sub>8</sub>-Tat), determined as the percentage of PTX recovered from the supernatant of DPBS solutions containing a mixture of PTX and conjugate. qC<sub>8</sub>-Tat shows the highest drug encapsulation efficiency among the three conjugates. (e) Variation of the loading capacity and encapsulation efficiency of qC<sub>8</sub>-Tat, with respect to PTX, as a function of the conjugate/PTX ratio. All the data in (d) and (e) are presented as the mean  $\pm$  SD ( $n = 3$ ).

pretreated with hexafluoro-2-propanol to achieve molecular level mixing, resulting in a typical DLC of nearly 7% due to the entrapment of PTX in the hydrophobic domain.

## RESULTS AND DISCUSSION

**Conjugate Characterization.** The purities of the three conjugates were all above 99% according to analytical HPLC analysis (Figures S1–S3 in Supporting Information (SI)). According to the MALDI-TOF mass spectra, the *m/z* of mC<sub>8</sub>-Tat, dC<sub>8</sub>-Tat, and qC<sub>8</sub>-Tat were observed to be 1843.826, 2098.104, and 2606.608 Da, respectively, in agreement with the expected exact masses of the three conjugates (1843.172 Da calculated from C<sub>78</sub>H<sub>146</sub>N<sub>36</sub>O<sub>16</sub>, 2097.371 Da calculated from C<sub>92</sub>H<sub>172</sub>N<sub>38</sub>O<sub>18</sub>, and 2605.770 Da calculated from C<sub>120</sub>H<sub>224</sub>N<sub>42</sub>O<sub>22</sub>).

**Self-Assembly.** We presume the number of hydrophobic tails will affect the self-assembly behavior of the Tat peptide conjugates. We therefore first carried out transmission electron microscopy (TEM) imaging to identify the possible nanostructures assembled from each conjugate in their respective aqueous solutions (2 mM, Dulbecco's phosphate-buffered saline (DPBS), pH 7.4). Self-assembly of the studied molecules was initiated by direct dissolution of each conjugate into the buffered solution. We found that only qC<sub>8</sub>-Tat can self-assemble into filamentous nanostructures (Figure 1b)

under these conditions, with no well-defined nanostructures observed for either dC<sub>8</sub>-Tat or mC<sub>8</sub>-Tat.

The wide-angle X-ray scattering pattern collected directly from aqueous solutions of Tat nanofibers reveals a strong reflection corresponding to a *d*-spacing of 4.7  $\text{\AA}$  (Figure S4 in SI). This reflection, frequently observed in nearly all amyloid and peptide fibrils and generally regarded as a  $\beta$ -sheet signature,<sup>55</sup> represents the distance between Tat peptides along the hydrogen-bonding direction. Tirrell and co-workers have shown that conjugation of a hydrocarbon tail to a short peptide can change its secondary structure from  $\alpha$ -helix (intramolecular hydrogen bonding) to  $\beta$ -sheets (intermolecular hydrogen bonding).<sup>56</sup> It is very likely that attachment of four hydrocarbon tails alters the Tat peptide's conformation and facilitates the formation of intermolecular hydrogen bonding. However, the corresponding circular dichroism (CD) spectrum shows no presence of the characteristic  $\beta$ -sheet signal but rather suggests a peptide conformation similar to polyproline II (PPII) helices, as evident by the negative peak around 205 nm (Figure 1c).<sup>57,58</sup> It is not clear to us how exactly the Tat peptides with a PPII-like conformation could form intermolecular hydrogen bonding and pack into 1D nanostructures. One plausible explanation could be that part of the Tat peptide adjacent to the C<sub>8</sub> tail forms intermolecular hydrogen bonding for the observed one dimensionality, while the rest of the Tat segment containing the PPQ residues and

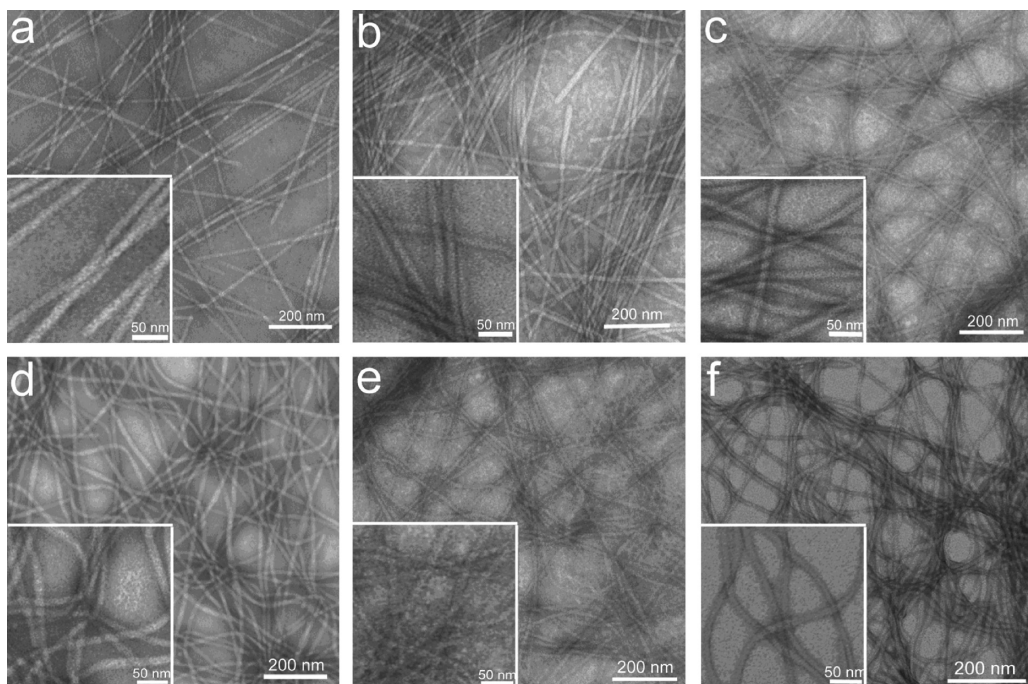


**Figure 2.** TEM study of the effect of PTX encapsulation on the nanofiber morphology. (a–f) TEM images of nanofibers formed in 2 mM solution of qC<sub>8</sub>-Tat only (a) and mixtures of qC<sub>8</sub>-Tat (2 mM) and PTX (b–f) with molar ratios of 100:1 (b), 20:1 (c), 10:1 (d), 20:3 (e), and 5:1 (f) after overnight equilibration in DPBS. The inset images are the enlargement of each respective image. More TEM images can be found in the SI (Figures S5–S10).

presented on the nanofiber periphery assumes a PPII-like conformation, which is mainly responsible for the observed CD signals. Validation of this hypothesis would require further studies and is beyond the scope of this work.

**Drug Encapsulation.** Next we carried out PTX encapsulation efficiency (EE) experiments using the three designed conjugates. We first dissolved PTX and the conjugate at two different molar mixing ratios (1:100 and 1:20) in hexafluoro-2-propanol (HFIP) to achieve molecular level mixing. After removal of the solvent using rotary evaporation, the mixture was redissolved in DPBS to reach a concentration of 2 mM with respect to the conjugate, and the EE was then determined using HPLC. The results in Figure 1d clearly show that for both mixing ratios the qC<sub>8</sub>-Tat conjugate exhibits the highest EE. This was not unexpected given its ability to assemble into nanofibers with a hydrophobic compartment. Both mC<sub>8</sub>-Tat and dC<sub>8</sub>-Tat conjugates show very poor ability to encapsulate PTX, except for dC<sub>8</sub>-Tat at the low mixing ratio (1:100) that can encapsulate 45% of PTX. In this case, it is likely that dC<sub>8</sub>-Tat is acting as a surfactant that enhances PTX's apparent solubility, much like Cremophore EL. The mC<sub>8</sub>-Tat may be too hydrophilic, and therefore no discernible drug encapsulation or solubilization effect was observed. Consequently, we evaluated the potential of using only qC<sub>8</sub>-Tat as a drug carrier and transporter in the following experiments.

We investigated the DLC of the qC<sub>8</sub>-Tat by mixing various amounts of paclitaxel (qC<sub>8</sub>-Tat:PTX = 100:1,

20:1, 10:1, 20:3, and 5:1, mol/mol) with the conjugate in HFIP using the same method described above. Figure 1e shows that the drug loading capacity was improved as more PTX was used for encapsulation. At the same time, the EE remained high (>95%) at low drug feeding ratios but dropped significantly when the added PTX exceeded the nanofiber's encapsulation capacity. The DLC and the corresponding EE at the highest ratio of drug to conjugate were  $6.8 \pm 0.4\%$  and  $89.7 \pm 5.0\%$ , respectively (Figure 1e). This observed DLC (nearly 7%) is impressively high in comparison to the reported values in most PTX-loaded nanomedicines, which rarely exceed 5%.<sup>10,46–49</sup> Moreover, the preparation procedure described here is rather simple, and no dialysis or other specific treatments were involved.

**Effect of Drug Encapsulation on Nanofiber Stiffness.** Upon encapsulation of PTX into the qC<sub>8</sub>-Tat nanofibers, we carried out further TEM imaging experiments, unexpectedly observing that PTX loading seems to alter the nanofiber stiffness (Figure 2). Without PTX, the Tat conjugate assembled into rigid nanofibers with their persistence lengths estimated on the scale of a few micrometers, with curves and turns seldom observed (Figure 2a and Figure S5 in SI). With increasing PTX loading, the assembled nanofibers began to show greater curvature and fluctuation along their long axis (Figure 2b,c, Figures S6 and S7 in SI). When the molar feeding ratio of PTX to qC<sub>8</sub>-Tat reached or exceeded 1:10, PTX-loaded Tat nanofibers attained a wiggly-like morphology (Figure 2d–f and Figures S8–10 in SI). At the same time, we did not observe any noticeable

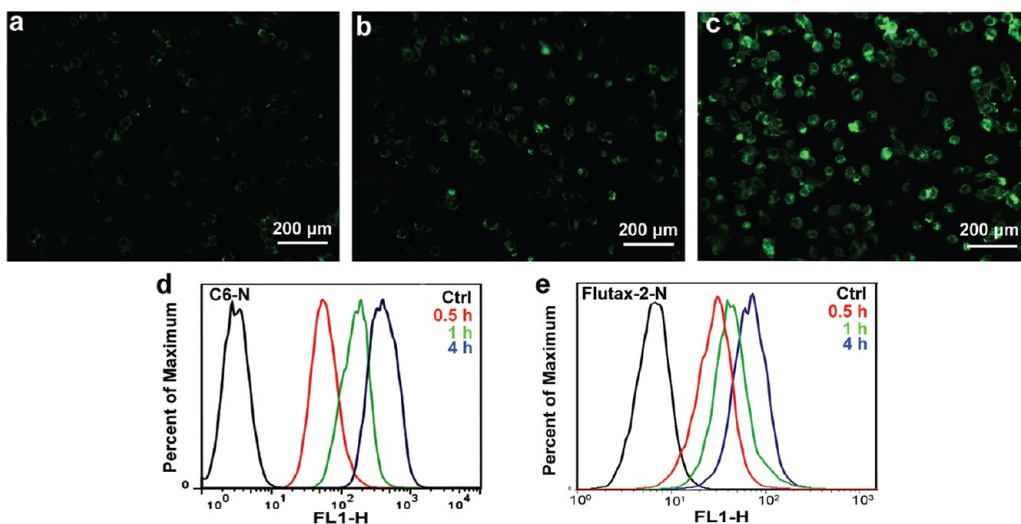


**Figure 3.** Cellular uptake of coumarin-6-loaded nanofibers by KB-3-1 cervical cancer cells. (a–c) Epifluorescence images of KB-3-1 cells after incubation with coumarin-6-loaded nanofibers (0.3  $\mu$ M coumarin-6 and 3  $\mu$ M qC<sub>8</sub>-Tat) for 0.5 h (a), 1 h (b), and 4 h (c). (d) Corresponding time-course fluorescence intensity of coumarin-6-loaded nanofibers treated cells determined by flow cytometry. (e) Time-course fluorescence intensity of KB-3-1 cells after incubation with Flutax-2-loaded nanofibers (0.5  $\mu$ M Flutax-2 and 5  $\mu$ M qC<sub>8</sub>-Tat) for 0.5, 1, and 4 h determined by flow cytometry. Cells incubated in media only were used as control (Ctrl).

change in nanofiber diameter. The mean diameters of the Tat nanofiber and nanofibers loaded with different amounts of PTX (100:1, 20:1, 10:1, 20:3, and 5:1, qC<sub>8</sub>-Tat: PTX, mol/mol) were consistently around 15 nm (Table S1 in SI). Although it has been shown in the literature that drug loading can alter the carrier's properties including size,<sup>59</sup> drug release rate,<sup>60</sup> and biodistribution,<sup>61</sup> to the best of our knowledge, this TEM observation presents the first evidence that drug loading could change the nanofiber stiffness.

In order to determine if the observed change in nanofiber stiffness stems from a conformational change in the Tat peptide, we collected CD spectra from an aqueous solution containing PTX-loaded nanofibers (PTX-N, Figure S11 in SI). We found it to be very similar to that of Tat nanofibers without PTX, suggesting that Tat peptides adopt the same conformation and are not responsible for the observed change in nanofiber morphology. Given the hydrophobic nature of PTX and similarity of CD spectra from blank nanofibers and PTX-N, we speculate that PTX would be entrapped into the hydrophobic cores of the assembled Tat nanofibers. Therefore, the most possible explanation for the altered stiffness after PTX loading could be linked to the effect of PTX on the hydrocarbon packing in the nanofiber core. Hsu *et al.* have shown that the palmitoyl hydrocarbon segments are packed with a high degree of order within the hydrophobic cores of the peptide amphiphile nanofibers.<sup>43</sup> It is very likely that the encapsulated bulky PTX disrupts the packing order of the hydrocarbons, thereby leading to the observed change in nanofiber stiffness.

**Cellular Uptake.** Since qC<sub>8</sub>-Tat nanofibers are able to solubilize PTX to a great extent (around 400  $\mu$ M in DPBS),

we evaluated their ability to transport hydrophobic molecules into cancer cells. Coumarin-6 was chosen as the model dye because of its strong fluorescence (quantum yield 0.8 in ethanol<sup>62</sup>) and low solubility in water ( $\sim$ 20 nM<sup>63</sup>). Coumarin-6 was loaded into Tat nanofibers using the same procedure as for PTX loading. The coumarin-6-loaded nanofibers (C6-N) were then incubated with KB-3-1 cervical cancer cells for a desired period of time before epifluorescence images were taken. Figure 3a–c show the time-dependent cellular uptake of coumarin-6 into cancer cells, evidenced by the stronger green fluorescence in the cells with longer incubation time. These results were further confirmed quantitatively by flow cytometry measurements, again revealing a consistent increase in fluorescence intensity when the incubation time changed from 0.5 to 4 h (Figure 3d and Figure S12 in SI, Geo means of the fluorescence intensity for cells incubated with nanofibers for 0.5, 1, and 4 h were 57.1, 156, and 391, respectively). Free coumarin-6, on the other hand, accumulated in the cells in a much different manner, with the intensity reaching a plateau in 1 h (Figure S12 in SI). This suggests that free coumarin-6 can diffuse freely into the cells and establish a quick equilibrium within 1 h. The coumarin-6 accumulation in C6-N-treated KB-3-1 cells proceeds at a slower rate; however, after 4 h the overall intensity is comparable to that in free coumarin-6-treated cells.

Given the smaller size of coumarin-6 relative to that of PTX, one may wonder whether it can truly represent PTX. Therefore cellular uptake of a paclitaxel–fluorophore conjugate, Flutax-2 (paclitaxel–Oregon Green 488 conjugate, Invitrogen), was also determined. Flutax-2 was chosen because it has been proven to retain both the affinity and specificity of PTX to

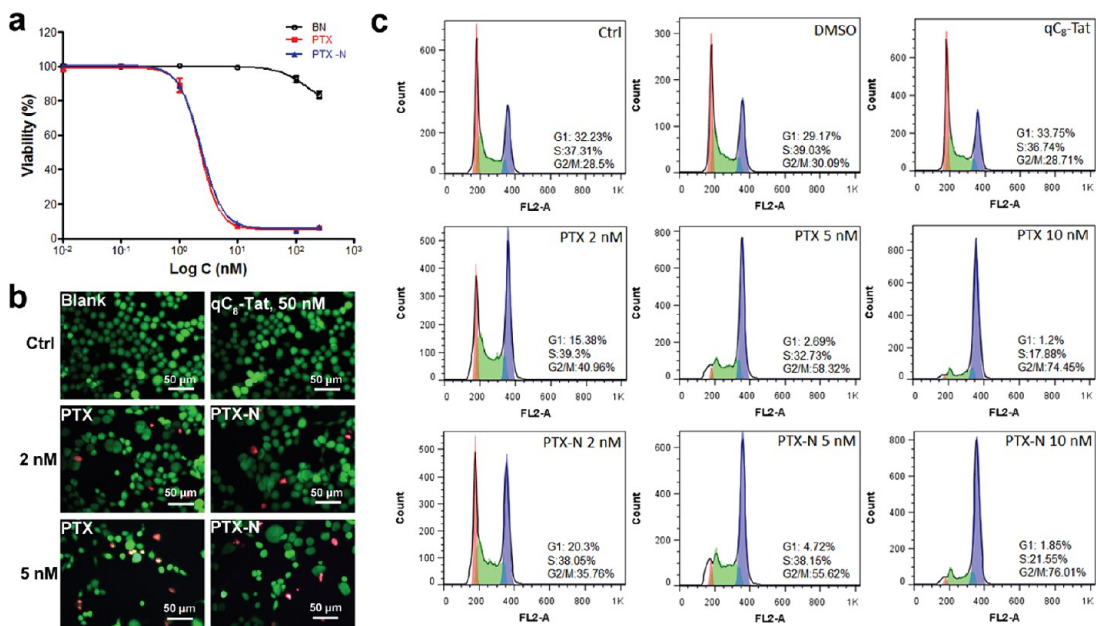


**Figure 4. Cytotoxicity and cell cycle studies of PTX-N-treated KB-3-1 cells.** (a) Cell viability at 48 h of KB-3-1 cells incubated with qC<sub>8</sub>-Tat, PTX, or PTX-N (qC<sub>8</sub>-Tat:PTX = 10:1, mol/mol), as determined by a sulforhodamine B-based method (SRB). Concentrations ranged from 0.01 to 250 nM for PTX and 0.1 to 2500 nM for qC<sub>8</sub>-Tat. (b) Cytotoxicity determined by Calcein AM/EthD-1 (live/dead, green/red) staining method after 48 h treatment with 2 and 5 nM PTX or PTX-N using nontreated cells or cells treated with 50 nM qC<sub>8</sub>-Tat as control. (c) Cell cycle distribution of KB-3-1 cells after 12 h incubation in medium only (Ctrl), DMSO (0.5% v/v), qC<sub>8</sub>-Tat (100 nM), PTX (2, 5, and 10 nM), or PTX-N (2, 5, and 10 nM) recorded by flow cytometry after staining with propidium iodide. The result reveals G2/M cell cycle arrest was the main mechanism of action of PTX-N.

microtubulules in live cells<sup>64,65</sup> and was used as an equivalent of PTX in drug delivery.<sup>66–68</sup> Similar to that of C6-N, the cellular uptake of Flutax-2-loaded nanofibers (Flutax-2-N) determined by flow cytometry is also time-dependent (Figure 3e). However, in this case, the intracellular accumulation of free Flutax-2 is 3–5 times lower than that of Flutax-2-N (Figure S13 in SI), in sharp contrast with the free coumarin-6 and C6-N pair, in which coumarin-6 accumulates much faster than C6-N (Figure S12 in SI). These experiments suggest that the cellular uptake of encapsulated drugs is primarily determined by the physicochemical properties of the nanocarriers, not by the molecular characteristics of the respective free drug.

It should be noted that flow cytometry measures the overall fluorescence from the whole cell regardless of its subcellular distribution. To assess any differences in the distribution between free and encapsulated drugs, we performed co-localization experiments, revealing that the majority of free coumarin-6 was actually trapped within the cell membrane, while C6-N was found largely inside the cells (*vida infra*). In the case of Flutax-2, the free molecule showed very poor cellular accumulation, while Flutax-2-N was found to be predominantly trapped in the lysosomes with much improved cellular uptake efficiency. These results clearly suggested that Tat nanofibers could efficiently transport hydrophobic molecules into cancer cells in a time-dependent and active manner not through free diffusion.

**Cytotoxicity of PTX-N and Cell Cycle Analysis.** Given the effectiveness of transporting hydrophobic molecules

into KB-3-1 cancer cells by Tat nanofibers, we carried out the cytotoxicity experiments to further evaluate the anticancer activity of PTX-N on KB-3-1 and on three other cell lines of different origins. The PTX-N samples used for cell toxicity studies were instantly diluted from a 2 mM stock solution that was prepared beforehand. Figure 4a shows that the IC<sub>50</sub> value of PTX-N against KB-3-1 cancer cells is nearly the same as that of pure PTX. Similar IC<sub>50</sub> values were observed for the other three cancer cell lines (Figures S14–S16 in SI), indicating that encapsulation did not reduce the efficacy of PTX. It is also worth mentioning here that qC<sub>8</sub>-Tat alone did not contribute to the cytotoxicity significantly over the concentration range (0.1–2500 nM) tested (Figure 4a and Figures S14–S16 in SI).

To confirm the observed efficacy further, cells with or without drug treatment were stained with solutions containing a mixture of calcein AM and ethidium homodimer-1 (EthD-1). Calcein AM can penetrate the cell membrane freely and be converted to membrane-impermeable green-fluorescent calcein after acetoxymethyl ester hydrolysis by intracellular esterases, while EthD-1 (red) can penetrate only the nonintegrated cell membrane and thus will stain only dead cells. After PTX or PTX-N treatment, the number of live cells (cells with green fluorescence) was significantly reduced compared with cells without any treatment or treated with only qC<sub>8</sub>-Tat, while at the same time an increased number of dead cells (cells with red fluorescence) was observed (Figure 4b). PTX and PTX-N showed comparable concentration-dependent

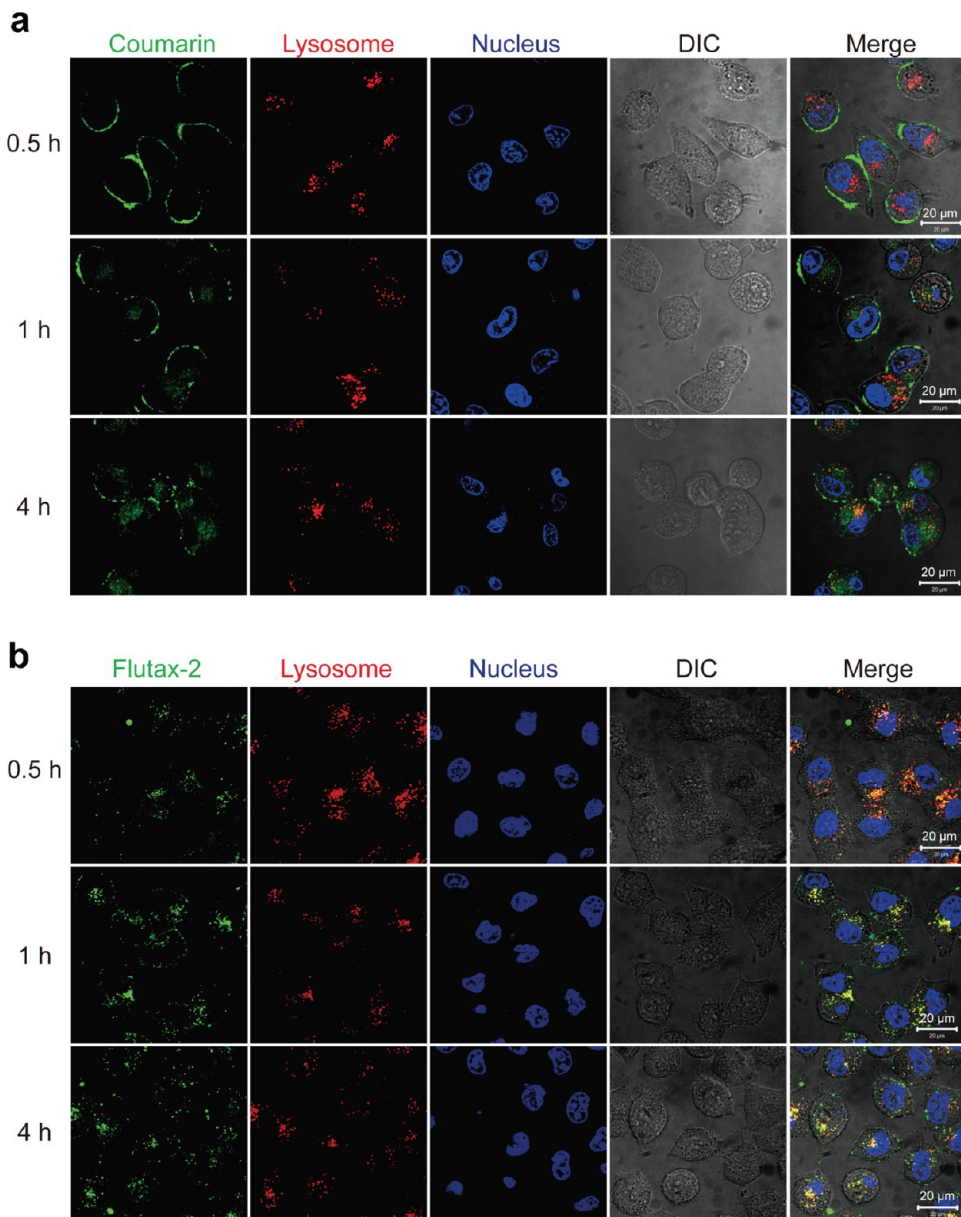


**Figure 5.** Live cell fluorescence imaging of drug-loaded-nanofiber-treated KB-3-1 cells. (a) Subcellular co-localization of qC<sub>8</sub>-Tat-delivered coumarin-6 (green) with lysosome (Lysotracker red, red) and the nucleus (Hoechst 33342, blue) after incubating KB-3-1 cells with 0.3  $\mu$ M coumarin-6 (3  $\mu$ M qC<sub>8</sub>-Tat) for 0.5, 1, and 4 h at 37 °C. (b) Subcellular co-localization of qC<sub>8</sub>-Tat-delivered Flutax-2 (green) with lysosome (Lysotracker red, red) and the nucleus (Hoechst 33342, blue) after incubating KB-3-1 cells with 0.5  $\mu$ M coumarin-6 (5  $\mu$ M qC<sub>8</sub>-Tat) for 0.5, 1, and 4 h at 37 °C.

cytotoxicity against KB-3-1 cancer cells (Figure 4b), consistent with the results from the SRB assay.

It has been reported that nanostructure-loaded drugs can exhibit an altered action mechanism due to changes in the intracellular concentration<sup>69</sup> or subcellular localization of the drugs.<sup>70</sup> Since the main mechanism of action of PTX against cancer cells is the cell cycle arrest at the G2/M phase induced by stabilized microtubules that could further lead to cell apoptosis,<sup>44</sup> we performed experiments to map out the distributions of treated cells in different mitotic phases. Figure 4c reveals that cells treated with PTX or PTX-N exhibited similar concentration-dependent

G2/M phase arrest. These experiments suggest a similar antitumor activity between PTX-N and free PTX. In both cases, a sharp transition was observed between cells treated with 2 and 5 nM drugs, and the observed high percentage of cells blocked at the G2/M phase (blue peak) correlates well with the high cytotoxicity (Figure 4a and b). These experiments also provide evidence that the Tat conjugate itself does not affect the mitosis of cells.

**Subcellular Localization.** In order to investigate the possible pathways through which the Tat nanofibers transport hydrophobic molecules into cells, confocal microscopy imaging was carried out to track the time-resolved

subcellular distribution of coumarin-6- or Flutax-2-loaded Tat nanofibers. In the cell experiments using C6-N, we found that the green fluorescence first appears on the cell membrane (0.5 h) and over time begins to emerge within the cells (Figure 5a). Partial co-localization with lysosomes was seen, but no coumarin-6 fluorescence within the nucleus could be observed. Similar phenomena were observed for Flutax-2-loaded Tat nanofibers. The green fluorescence from Flutax-2 was found both on the cell membrane and in the cells at all observed time points, and nearly all the green fluorescence in the cells co-localized with red fluorescence from lysosomes (Figure 5b).

Given the observed changes in fluorescence intensity and location with time, we speculate that the Tat nanofibers transport their cargos (either coumarin-6 or Flutax-2) into cells through the adsorptive-mediated endocytosis (AME) pathway. It is very likely that the nanofibers would first interact with the cell membrane through electrostatic attractions between positively charged Tat peptides and the negatively charged cell membrane. The AME mechanism could then be initiated either by the intact nanofibers<sup>71</sup> or by the dissociated qC<sub>8</sub>-Tat conjugates on the cell membrane.<sup>72</sup> In either case, coumarin-6 or Flutax-2 can be transported into cells through the AME-associated membrane internalization event.<sup>73</sup> This mechanism was supported by the observation of granular green dots and the co-localization of the green fluorescence with lysosomes. In addition, these experiments suggest again that the cellular uptake mechanism is primarily linked to the properties of the carrier (the Tat nanofiber), independent of the molecular characteristics of the cargo encapsulated.

This similarity in endocytosis pathway of using Tat nanofibers to transport coumarin-6 and Flutax-2 into cells is in sharp contrast with the difference in cellular uptake behaviors of the individual free molecules. Both free coumarin-6 and Flutax-2 showed reduced intracellular accumulation but differ in their subcellular distribution. In the case of free coumarin-6, although both fluorescence and flow cytometry experiments showed improved coumarin-6 concentration within cells (Figures S12 and S17 in SI), confocal imaging clearly revealed that most coumarin-6 was actually trapped within the cell membranes (Figure S17 in SI). The low intracellular accumulation of coumarin-6 was possibly due to its tendency to remain in the hydrophobic environment of the cell membrane.<sup>74</sup> The observation of intense fluorescence on the cell membrane and poor accumulation within cells suggests passive diffusion as the major cellular uptake mechanism. In the case of free Flutax-2, we observed a significantly reduced Flutax-2 green fluorescence from free Flutax-2-treated cells in comparison with the Flutax-2-N-treated cells (Figure S18 in SI). Also, in contrast to the entrapment of coumarin-6 within cell membranes, no membrane retention was observed for Flutax-2. This is not surprising given the more hydrophilic nature of Flutax-2.

These experiments collectively suggest that passive diffusion seems to be the most plausible pathway for both coumarin-6 and Flutax-2 to gain access to cells, although we cannot exclude the possibility that other mechanisms such as spontaneous pinocytosis (the uptake of fluid and solutes) may also be involved in both free coumarin-6 and Flutax-2 cases.<sup>75,76</sup> For this passive diffusion mechanism, the molecule's partitioning and distribution in different cell components is primarily determined by the hydrophilic–lipophilic balance value (reflected by the logarithm of partition coefficient P (logP)) (*vida infra*).

On the basis of the effective transport of coumarin-6 and Flutax-2 into cells by Tat nanofibers, we believe that PTX-N should also be able to transport encapsulated paclitaxel into cells as efficiently (Figure 6). If the subcellular localization behaviors of free coumarin-6 or Flutax-2 are truly representative of that of free PTX, one would expect a much improved potency of PTX-N over free PTX against cancer cells because PTX-N would supposedly deliver much more PTX into cells. Therefore, it was surprising to observe that free PTX and PTX-N instead showed comparable cytotoxicity against the studied cancer cell lines.

We speculate that the observed comparable toxicity between PTX-N and free PTX can be attributed to both the PTX's better ability to penetrate the cell membrane and the delayed release of PTX from lysosomes for PTX-N. We reason that free PTX probably has a higher intracellular accumulation compared to free coumarin-6 and Flutax-2 due to their difference in the physicochemical properties (Figure 6). The logP may be the most important factor to estimate the molecule's ability to diffuse across the cell membrane, although other characteristics such as molecular weight and polar surface area will also have an effect.<sup>74,77,78</sup> The logP of coumarin-6, paclitaxel, and Flutax-2 at pH 7.4, as predicted by MarvinSketch (ver. 5.12.3, ChemAxon, MA), are 4.8 (reported experimental value 5.2<sup>79</sup>), 3.5 (reported experimental value 3.96<sup>80</sup>), and 1.2 (no experimental value available), respectively. A larger logP is believed to correlate with higher membrane retention and poor intracellular accumulation,<sup>81</sup> which is consistent with our observation for free coumarin-6. Molecules with smaller logP usually show lower cell membrane penetrating ability,<sup>74</sup> which is also in agreement with the cellular uptake result observed for free Flutax-2. PTX, with an experimental logP of 3.96, could possess better membrane permeability and intracellular accumulation than both coumarin-6 and Flutax-2, although this ability may be slightly compromised by its high molecular weight (>500 Da) and large polar surface area (>140 Å<sup>2</sup>).<sup>77,78</sup>

Although PTX-N most likely improves the intracellular accumulation of PTX, the retarded release of PTX from lysosomes through diffusion could potentially affect its potency. Following the AME pathway, the PTX-N would be engulfed into endosomes. Upon fusion of the endosome with the lysosome, the

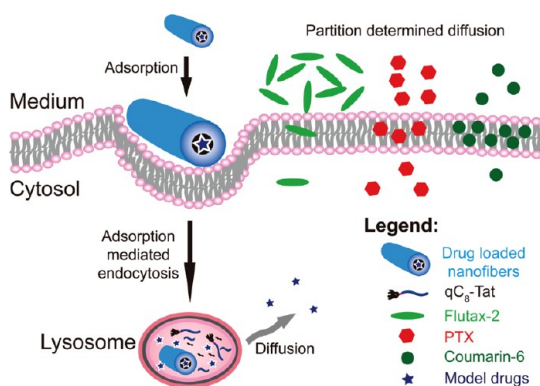


**Figure 6. Proposed endocytosis mechanisms of drug-loaded nanofibers and free drugs.** Tat nanofibers, regardless of the properties of cargos loaded in the hydrophobic core, can be actively endocytosed through the proposed adsorption-mediated endocytosis pathway, and the encapsulated drugs can diffuse out of the lysosome after the disassembly of the nanofibers. The intracellular accumulation of free drug was largely determined by the logarithm of the partition coefficient  $P$  ( $\log P$ ). Flutax-2, which has a very small  $\log P$  value (1.2), cannot penetrate the cell membrane efficiently. Coumarin-6, with a large  $\log P$  value (5.2), shows strong affinity to the cell membrane and thus is trapped in the membrane. Paclitaxel, with its  $\log P$  (3.96) between those of Flutax-2 and coumarin-6, can effectively diffuse across the cell membrane and achieve considerable intracellular accumulation.

decrease of pH, degradation of  $qC_8$ -Tat by enzymes, dilution of the nanofibers, and also interaction of nanofibers with the lysosome membrane would all act together to destabilize the nanofibers and trigger the release of encapsulated cargos. The ability of PTX to diffuse across the lysosomal membrane into cytosol can be inferred from the subcellular localization experiments

using Flutax-2-N because the  $\log P$  of Flutax-2 at  $pH \sim 5.5$  (lysosome-related pH) is predicted to be 3.92 (MarvinSketch software), a value close to that of PTX. The observed entrapment of Flutax-2-N in lysosomes may explain the retarded release of free PTX from PTX-N within the lysosomes. Therefore, we hypothesize that the Tat nanovector can be further optimized with the inclusion of the lysosome escape property, allowing for improved efficacy regardless of the physicochemical properties of encapsulated model drugs.

## CONCLUSION

In conclusion,  $qC_8$ -Tat nanofibers can be used to efficiently encapsulate paclitaxel through the facile procedure of dissolving the premixed drug and the self-assembling Tat conjugate in an aqueous solution. These PTX-loaded nanofibers can effectively transport hydrophobic molecules into cancer cells through an adsorptive-mediated pathway and exhibited potent efficacy on multiple cancer cell lines *in vitro* by inducing G2/M phase cell cycle arrest. The PTX-loaded nanofibers may present a promising PTX formulation for cancer chemotherapy. Furthermore, the Tat nanofiber could serve as an ideal drug carrier for molecules with poor ability for membrane penetration. Given the fact that modern new drug discovery strategies mainly pick out candidates that show efficacy in their free form,<sup>82</sup> introducing nanocarriers into the *in vitro* screening process could allow for identifying compounds that cannot enter cells in their free form but exhibit potent efficacy upon assisted entry into cells by the carrier.

## MATERIALS AND METHODS

**Materials.** All Fmoc amino acids unless stated otherwise were purchased from Advanced Automated Peptide Protein Technologies (AAPTEC, Louisville, KY, USA), and Rink amide MBHA and Fmoc-Lys(Fmoc) were obtained from Novabiochem (San Diego, CA, USA). Coumarin-6 was purchased from ACROS Organics (Fairlawn, NJ, USA), and paclitaxel was sourced from Avachem Scientific LLC (San Antonio, TX, USA). Flutax-2 (paclitaxel, Oregon Green 488 conjugate) and live/dead cell viability assay kits were purchased from Invitrogen (Grand Island, NY, USA). All other reagents were obtained from VWR (Radnor, PA, USA) and used as received without further purification.

**Cell Culture.** KB-3-1 cervical cancer cell lines and MDA-MD-231 breast cancer cell line were kindly provided by Dr. Gottesman (Center for Cancer Research, National Cancer Institute) and Dr. Konstantopoulos (ChemBE, JHU), respectively. DMEM (Invitrogen) containing 10% fetal bovine serum (FBS, Invitrogen) and 1% antibiotics (Invitrogen) was used for the culture of these two cell lines. The A549 non-small-cell lung cancer cell line was kindly provided by Dr. Hanes (SOM, JHU) and was grown in Advanced RPMI1640 medium (Invitrogen) containing 1% FBS, 1% antibiotics, 2 mM L-glutamine, and 10 mM 4-(2-hydroxyethyl)-1-piperazineethanesulfonic acid. The OVCAR-8 ovarian cancer cell line was purchased from the National Cancer Institute and was grown in RPMI 1640 containing 10% FBS, 1% antibiotics, and 2 mM L-glutamine. All cell types were incubated at 37 °C in a humidified incubator with a 5% CO<sub>2</sub> atmosphere (Oasis, Caron, Marietta, OH, USA).

**Tat Conjugates Synthesis and Characterization.** All peptide conjugates were synthesized using standard 9-fluorenylmethoxy-carbonyl (Fmoc) solid phase synthesis techniques. The peptides Fmoc-GRK<sub>2</sub>R<sub>2</sub>QR<sub>3</sub>P<sub>2</sub>Q-Rink, Fmoc-K(Fmoc)GRK<sub>2</sub>R<sub>2</sub>QR<sub>3</sub>P<sub>2</sub>Q-Rink, and (Fmoc-K(Fmoc))KGRK<sub>2</sub>R<sub>2</sub>QR<sub>3</sub>P<sub>2</sub>Q-Rink were synthesized on a 0.25 mmol scale using the Focus XC automated peptide synthesizer (AAPTEC, Louisville, KY, USA). Octanoic acid (C<sub>8</sub>) was coupled at the lysine N-terminal and side-chain amines (after Fmoc removal) at room temperature. In all cases, reactions were monitored by the ninhydrin test (Anaspec Inc., Fremont, CA, USA) for free amines. Completed peptides were cleaved from the solid support using a mixture of TFA/TIS/H<sub>2</sub>O in a ratio of 95:2.5:2.5 for 3 h. Excess TFA was removed by rotary evaporation, and cold diethyl ether was added to precipitate the crude products, which were collected and dried under vacuum overnight.

All the conjugates were purified by preparative RP-HPLC using a Varian ProStar model 325 HPLC (Agilent Technologies, Santa Clara, CA, USA) equipped with a fraction collector. Separations were performed using a Varian PLRP-S column (100 Å, 10 μm, 150 × 25 mm) monitoring at 220 nm. Collected fractions were analyzed by ESI-MS (LDQ Deca ion-trap mass spectrometer, Thermo Finnigan, USA), and those containing the target molecules were combined and lyophilized (FreeZone –105 °C, Labconco, Kansas City, MO, USA) and then stored at –30 °C. The purity of the conjugates was analyzed by HPLC using the following conditions: Agilent Zorbax-C<sub>18</sub> column (5 μm, 4.6 × 150 mm); the flow rate was 1 mL/min, with the mobile phase

starting from 15% MeCN (with 0.1% TFA) and 85% 0.1% TFA aqueous solution at 2 min to 70% MeCN (with 0.1% TFA) at 12 min, hold for 3 min, gradient back to the initial conditions in 1 min, and hold for 4 min; the monitored wavelength was 220 nm. High-resolution peptide masses were determined by MALDI-TOF mass spectrometry, using an Autoflex III MALDI-TOF instrument (Bruker, Billerica, MA, USA). Samples were prepared by depositing 1  $\mu$ L of sinapinic acid matrix (10 mg/mL in 0.05% TFA in H<sub>2</sub>O/MeCN (1:1), Sigma-Aldrich, PA, USA) onto the target spot and allowing to dry for 5 min. Then 1  $\mu$ L of aqueous peptide solution (0.1% TFA) was deposited on the corresponding spot and quickly mixed with 1  $\mu$ L of sinapinic acid matrix solution before air drying. Samples were irradiated with a 355 nm UV laser and analyzed in the reflectron mode.

**Paclitaxel Encapsulation.** The drug encapsulation experiments were performed as follows: paclitaxel (100:1 or 20:1, mol/mol) and the appropriate conjugate (4  $\times$  10<sup>-7</sup> mol) were dissolved in 100  $\mu$ L of HFIP in 2 mL glass vials and sonicated for 1 min to mix, before the HFIP was removed by rotary evaporation. The vials were then left to stand in the fume hood for at least 8 h at room temperature with the cap removed to allow any trace amount of HFIP to evaporate. Then 200  $\mu$ L of 1  $\times$  DPBS was added to each vial and vortexed for 30 s. The solutions were aged for 8 h and then centrifuged (2000g, 5 min) to remove any precipitated PTX, and the supernatant was carefully collected and analyzed using HPLC with the following conditions: Varian ProStar model 325 HPLC (Agilent Technologies, Santa Clara, CA, USA) equipped with an Agilent Zorbax-C<sub>18</sub> column (5  $\mu$ m, 4.6  $\times$  150 mm); the flow rate was 1 mL/min, with the mobile phase held at 35% A (MeCN with 0.1% TFA) and 65% B (0.1% TFA aqueous solution) for 5 min and start to gradient to 70% A at a period of 25 min, then gradient back to the initial conditions in 1 min and held for 4 min; the monitored wavelength was 237 nm. The drug encapsulation efficiency was calculated as the percentage of paclitaxel recovered from the supernatant to the paclitaxel added. The drug loading capacity was calculated from the percentage of recovered paclitaxel to the sum of recovered paclitaxel and added conjugates.

**Self-Assembly and Characterization.** To observe the morphology of nanostructures formed by qC<sub>8</sub>-Tat, transmission electron microscopy imaging was performed. The nanomedicines were prepared as described above at a qC<sub>8</sub>-Tat concentration of 2 mM with various PTX concentrations (from 0 to 400  $\mu$ M) and aged overnight. TEM samples were prepared by depositing 5  $\mu$ L of the samples onto a carbon-coated copper grid (Electron Microscopy Services, Hatfield, PA, USA), wicking away excess solution using filter paper, and drying for 10–15 min. Negative staining was carried out by adding 5  $\mu$ L of a 2 wt % uranyl acetate aqueous solution, wicking away excess solution using filter paper, and drying for at least 3 h at room temperature. Bright-field TEM imaging was performed on a FEI Tecnai 12 TWIN transmission electron microscope operated at an acceleration voltage of 100 kV. All TEM images were recorded by a SIS Megaview III wide-angle CCD camera.

**Circular Dichroism (CD) Measurement.** The CD spectra of the qC<sub>8</sub>-Tat and PTX-loaded qC<sub>8</sub>-Tat were obtained using the following protocol: 16  $\mu$ L of qC<sub>8</sub>-Tat with or without paclitaxel (10:1, mol/mol) was dissolved in 100  $\mu$ L of HFIP, sonicated, and dried using a Rotavapor. Then 400  $\mu$ L of DPBS was added to dissolve the conjugate and paclitaxel. The solution was aged for 24 h, and the CD spectrum was recorded on a J-710 spectropolarimeter (JASCO, Easton, MD, USA) from 195 to 280 nm. The signal was converted from ellipticity (mdeg) to mean molar ellipticity per residue (deg  $\cdot$  cm<sup>2</sup>  $\cdot$  dmol<sup>-1</sup>  $\cdot$  residue<sup>-1</sup>).

**Cellular Uptake and Subcellular Localization.** The cellular uptake experiment was performed on KB-3-1 cervical cancer cells qualitatively and quantitatively. Coumarin-6 was selected as a model drug because of its hydrophobicity, strong green fluorescence, and wide application in the *in vitro* and *in vivo* evaluation of drug delivery system.<sup>83,84</sup> Flutax-2 was also employed because of its similarity to PTX in structure<sup>64,65</sup> and previous successful application as a model drug in drug delivery.<sup>66–68</sup> Coumarin-6 or Flutax-2 and qC<sub>8</sub>-Tat were dissolved in HFIP at a ratio of 1 to 10 (mol/mol) and dried using a rotary evaporator under vacuum to give a thin film. Sterilized DPBS was added to dissolve the film to achieve a final coumarin-6

concentration of 30  $\mu$ M (50  $\mu$ M for Flutax-2 because of its lower fluorescence intensity), and the solution was aged overnight. KB-3-1 cells were seeded onto a 24-well plate at 1  $\times$  10<sup>5</sup> cells/well or on a collagen-pretreated eight-well glass-bottom plate (Lab-Tek, Thermo, NY, USA) at 4  $\times$  10<sup>4</sup> cells/well and allowed to attach overnight. Cells were then treated with fresh medium containing drug-loaded nanofibers or free drug (final coumarin-6 or Flutax-2 concentration at 0.3 or 0.5  $\mu$ M, respectively) for 0.5, 1, and 4 h and then washed twice with Hank's balanced salt solution. For fluorescence microscope imaging, cells were directly imaged using an epifluorescence microscope (Jenco, OR, USA) and a confocal laser scanning microscope (Zeiss 510, Germany). For the flow cytometry assay, cells were trypsinized, collected, washed, resuspended in DPBS, and analyzed using the FL1 channel (green) on a FACScalibur flow cytometer (Becton Dickinson, NJ, USA). Data were processed and compared using Flowjo software (version 7.6.5, Tree Star, OR, USA).

**Cytotoxicity.** The cytotoxicity of PTX-N was evaluated using the SRB method and live/dead stain imaging. KB-3-1, A549, MDA-MB-231, or OVCAR-8 cells were seeded onto 96-well plates (5  $\times$  10<sup>3</sup> cells/well) and allowed to attach overnight. Tat nanofibers and PTX-N were prepared at the same time and aged overnight. A 100  $\times$  PTX-N stock solution was then diluted with fresh medium and incubated with cells immediately to achieve final paclitaxel concentrations of 0.01, 0.1, 1, 10, 100, and 250 nM. Medium containing the same concentration of PTX or corresponding concentration of Tat nanofibers (0.1 nM to 2.5 mM) was also used to incubate the cells, with cells treated with solvent only as a control group. After 48 h incubation, the cell viability was determined using the SRB method according to the manufacturer's protocol (TOX-6, Sigma, St. Louis, MO, USA). In accordance with the results of the SRB method, live/dead imaging was conducted at 2 and 5 nM to confirm the cytotoxicity of the PTX-N. KB-3-1 cells were seeded onto a collagen-coated cover glass inserted 24-well plate (3  $\times$  10<sup>4</sup> cells/well) and allowed to attach overnight. The medium was replaced with fresh medium containing PTX, PTX-N, or a mixture of PTX and Tat nanofibers (2 and 5 nM paclitaxel) and incubated for 48 h. Cells treated with blank Tat nanofibers or medium only were used as control. The cells were stained using a live/dead viability/cytotoxicity kit for mammalian cells according to the manufacturer's protocol (Invitrogen).

**Cell Cycle Analysis.** To understand the antitumor mechanism of PTX-N, cell cycle analysis was performed on cells treated with PTX-N or free PTX. KB-3-1 cells were seeded onto a six-well plate (1.5  $\times$  10<sup>5</sup> cells/well) and allowed to attach overnight. The medium was then replaced with fresh medium containing 2, 5, or 10 nM PTX or PTX-N. Cells incubated with medium, 0.5% DMSO, or 100 nM qC<sub>8</sub>-Tat were used as control. After 12 h incubation, cells were collected, washed twice with DPBS, and fixed with 70% ethanol aqueous solution (−20 °C) overnight. The fixed cells were washed with DPBS three times and resuspended in 0.3 mL of DPBS before treatment with RNase A (0.1 mg/mL, Thermo Scientific Fermentas, Waltham, MA, USA) at 37 °C for 15 min. The cells were then stained with propidium iodide (20  $\mu$ g/mL, Invitrogen) in the dark at room temperature for 30 min. Analysis was performed using the FL2-A channel of a FACScalibur flow cytometer. The collected data were processed and compared using Flowjo software.

**Conflict of Interest:** The authors declare no competing financial interest.

**Supporting Information Available:** Additional characterization (HPLC and MALDI-TOF of the conjugates), WAXS data of qC<sub>8</sub>-Tat nanofibers, additional TEM images of nanofibers formed by qC<sub>8</sub>-Tat with or without PTX and their diameters, CD spectra of a blank nanofiber and a nanofiber with paclitaxel, cellular uptake of free coumarin-6, C6-N, Flutax-2, and Flutax-2-N, cytotoxicity data of paclitaxel-loaded nanofibers on A549, MDA-MB-231, and OVCAR-8, subcellular distribution of free coumarin-6 and Flutax-2 in KB-3-1 cells, and diameters of nanofibers with or without paclitaxel are provided. This material is available free of charge via the Internet <http://pubs.acs.org>.

**Acknowledgment.** The work reported here is supported by the National Science Foundation (DMR 1255281). We thank

National Institutes of Health (NIH) for funding A.C. (T-32CA130840) and Y.L. (R25 CA153952). The authors thank the Integrative Imaging Center (IIC) at the Johns Hopkins University for TEM and confocal imaging. The authors also thank Professor K. Konstantopoulos for the use of the flow cytometer, Professor H. Mao for the use of the plate reader, and Professor K. Hristova for the use of the CD spectropolarimeter.

## REFERENCES AND NOTES

1. Lindgren, M.; Hallbrink, M.; Prochiantz, A.; Langel, U. Cell-Penetrating Peptides. *Trends Pharmacol. Sci.* **2000**, *21*, 99–103.
2. Richard, J. P.; Melikov, K.; Vives, E.; Ramos, C.; Verbeure, B.; Gait, M. J.; Chernomordik, L. V.; Lebleu, B. Cell-Penetrating Peptides - a Reevaluation of the Mechanism of Cellular Uptake. *J. Biol. Chem.* **2003**, *278*, 585–590.
3. Deshayes, S.; Morris, M. C.; Divita, G.; Heitz, F. Cell-Penetrating Peptides: Tools for Intracellular Delivery of Therapeutics. *Cell. Mol. Life Sci.* **2005**, *62*, 1839–1849.
4. Zorko, M.; Langel, U. Cell-Penetrating Peptides: Mechanism and Kinetics of Cargo Delivery. *Adv. Drug Delivery Rev.* **2005**, *57*, 529–545.
5. Wang, J. T. W.; Giuntini, F.; Eggleston, I. M.; Bown, S. G.; MacRobert, A. J. Photochemical Internalisation of a Macromolecular Protein Toxin Using a Cell Penetrating Peptide-Photosensitiser Conjugate. *J. Controlled Release* **2012**, *157*, 305–313.
6. Boisguerin, P.; Redt-Clouet, C.; Franck-Miclo, A.; Lichehbe, S.; Nargeot, J.; Barrere-Lemaire, S.; Lebleu, B. Systemic Delivery of Bh4 Anti-Apoptotic Peptide Using CppS Prevents Cardiac Ischemia-Reperfusion Injuries *in Vivo*. *J. Controlled Release* **2011**, *156*, 146–153.
7. Gillmeister, M. P.; Betenbaugh, M. J.; Fishman, P. S. Cellular Trafficking and Photochemical Internalization of Cell Penetrating Peptide Linked Cargo Proteins: A Dual Fluorescent Labeling Study. *Bioconjugate Chem.* **2011**, *22*, 556–566.
8. Moschos, S. A.; Jones, S. W.; Perry, M. M.; Williams, A. E.; Erjefalt, J. S.; Turner, J. J.; Barnes, P. J.; Sproat, B. S.; Gait, M. J.; Lindsay, M. A. Lung Delivery Studies Using Sirna Conjugated to Tat(48–60) and Penetratin Reveal Peptide Induced Reduction in Gene Expression and Induction of Innate Immunity. *Bioconjugate Chem.* **2007**, *18*, 1450–1459.
9. Zhu, L.; Kate, P.; Torchilin, V. P. Matrix Metalloprotease 2-Responsive Multifunctional Liposomal Nanocarrier for Enhanced Tumor Targeting. *ACS Nano* **2012**, *6*, 3491–3498.
10. Tong, R.; Hemmati, H. D.; Langer, R.; Kohane, D. S. Photo-switchable Nanoparticles for Triggered Tissue Penetration and Drug Delivery. *J. Am. Chem. Soc.* **2012**, *134*, 8848–8855.
11. Xiong, X. B.; Lavasanifar, A. Traceable Multifunctional Micellar Nanocarriers for Cancer-Targeted Co-Delivery of Mdr-1 Sirna and Doxorubicin. *ACS Nano* **2011**, *5*, 5202–5213.
12. Wang, H. Y.; Xu, K. J.; Liu, L. H.; Tan, J. P. K.; Chen, Y. B.; Li, Y. T.; Fan, W. M.; Wei, Z. Q.; Sheng, J. F.; Yang, Y. Y.; et al. The Efficacy of Self-Assembled Cationic Antimicrobial Peptide Nanoparticles against Cryptococcus Neoformans for the Treatment of Meningitis. *Biomaterials* **2010**, *31*, 2874–2881.
13. Yoon, Y. R.; Lim, Y. B.; Lee, E.; Lee, M. Self-Assembly of a Peptide Rod-Coil: A Polyproline Rod and a Cell-Penetrating Peptide Tat Coil. *Chem. Commun. (Cambridge, U.K.)* **2008**, 1892–1894.
14. Lim, Y. B.; Lee, E.; Lee, M. Controlled Bioactive Nanostructures from Self-Assembly of Peptide Building Blocks. *Angew. Chem., Int. Ed.* **2007**, *46*, 9011–9014.
15. Li, S. D.; Huang, L. Pharmacokinetics and Biodistribution of Nanoparticles. *Mol. Pharmaceutics* **2008**, *5*, 496–504.
16. Geng, Y.; Dalheimer, P.; Cai, S. S.; Tsai, R.; Tewari, M.; Minko, T.; Discher, D. E. Shape Effects of Filaments versus Spherical Particles in Flow and Drug Delivery. *Nat. Nanotechnol.* **2007**, *2*, 249–255.
17. Decuzzi, P.; Godin, B.; Tanaka, T.; Lee, S. Y.; Chiappini, C.; Liu, X.; Ferrari, M. Size and Shape Effects in the Biodistribution of Intravascularly Injected Particles. *J. Controlled Release* **2010**, *141*, 320–327.
18. Park, J. H.; von Maltzahn, G.; Zhang, L. L.; Schwartz, M. P.; Ruoslahti, E.; Bhatia, S. N.; Sailor, M. J. Magnetic Iron Oxide Nanoworms for Tumor Targeting and Imaging. *Adv. Mater.* **2008**, *20*, 1630–1635.
19. Gratton, S. E. A.; Ropp, P. A.; Pohlhaus, P. D.; Luft, J. C.; Madden, V. J.; Napier, M. E.; DeSimone, J. M. The Effect of Particle Design on Cellular Internalization Pathways. *Proc. Natl. Acad. Sci. U.S.A.* **2008**, *105*, 11613–11618.
20. Muro, S.; Garnacho, C.; Champion, J. A.; Leferovich, J.; Gajewski, C.; Schuchman, E. H.; Mitragotri, S.; Muzykantov, V. R. Control of Endothelial Targeting and Intracellular Delivery of Therapeutic Enzymes by Modulating the Size and Shape of Icam-1-Targeted Carriers. *Mol. Ther.* **2008**, *16*, 1450–1458.
21. Lodge, T. P. Block Copolymers: Past Successes and Future Challenges. *Macromol. Chem. Phys.* **2003**, *204*, 265–273.
22. Israelachvili, J. N. *Intermolecular and Surface Forces*, 3rd ed.; Academic Press Limited, 2011.
23. Porte, G. Giant Micelles in Ideal Solutions - Either Rods or Vesicles. *J. Phys. Chem.* **1983**, *87*, 3541–3550.
24. Gref, R.; Minamitake, Y.; Peracchia, M. T.; Trubetskoy, V.; Torchilin, V.; Langer, R. Biodegradable Long-Circulating Polymeric Nanospheres. *Science* **1994**, *263*, 1600–1603.
25. Aida, T.; Meijer, E. W.; Stupp, S. I. Functional Supramolecular Polymers. *Science* **2012**, *335*, 813–817.
26. Pashuck, E. T.; Stupp, S. I. Direct Observation of Morphological Transformation from Twisted Ribbons into Helical Ribbons. *J. Am. Chem. Soc.* **2010**, *132*, 8819–.
27. Childers, W. S.; Mehta, A. K.; Ni, R.; Taylor, J. V.; Lynn, D. G. Peptides Organized as Bilayer Membranes. *Angew. Chem., Int. Ed.* **2010**, *49*, 4104–4107.
28. Cui, H.; Muraoka, T.; Cheetham, A. G.; Stupp, S. I. Self-Assembly of Giant Peptide Nanobelts. *Nano Lett.* **2009**, *9*, 945–951.
29. Schneider, J. P.; Pochan, D. J.; Ozbas, B.; Rajagopal, K.; Pakstis, L.; Kretsinger, J. Responsive Hydrogels from the Intramolecular Folding and Self-Assembly of a Designed Peptide. *J. Am. Chem. Soc.* **2002**, *124*, 15030–15037.
30. Zhang, Y.; Zhang, B.; Kuang, Y.; Gao, Y.; Shi, J.; Zhang, X. X.; Xu, B. A Redox Responsive, Fluorescent Supramolecular Metallohydrogel Consists of Nanofibers with Single-Molecule Width. *J. Am. Chem. Soc.* **2013**, *135*, 5008–5011.
31. Trent, A.; Marullo, R.; Lin, B.; Black, M.; Tirrell, M. Structural Properties of Soluble Peptide Amphiphile Micelles. *Soft Matter* **2011**, *7*, 9572–9582.
32. Cui, H. G.; Webber, M. J.; Stupp, S. I. Self-Assembly of Peptide Amphiphiles: From Molecules to Nanostructures to Biomaterials. *Biopolymers* **2010**, *94*, 1–18.
33. Hartgerink, J. D.; Beniash, E.; Stupp, S. I. Peptide-Amphiphile Nanofibers: A Versatile Scaffold for the Preparation of Self-Assembling Materials. *Proc. Natl. Acad. Sci. U.S.A.* **2002**, *99*, 5133–5138.
34. Branco, M. C.; Sigano, D. M.; Schneider, J. P. Materials from Peptide Assembly: Towards the Treatment of Cancer and Transmittable Disease. *Curr. Opin. Chem. Biol.* **2011**, *15*, 427–434.
35. Zhang, S. G. Lipid-Like Self-Assembling Peptides. *Acc. Chem. Res.* **2012**, *45*, 2142–2150.
36. Banwell, E. F.; Abelardo, E. S.; Adams, D. J.; Birchall, M. A.; Corrigan, A.; Donald, A. M.; Kirkland, M.; Serpell, L. C.; Butler, M. F.; Woolfson, D. N. Rational Design and Application of Responsive Alpha-Helical Peptide Hydrogels. *Nat. Mater.* **2009**, *8*, 596–600.
37. O'Leary, L. E. R.; Fallas, J. A.; Bakota, E. L.; Kang, M. K.; Hartgerink, J. D. Multi-Hierarchical Self-Assembly of a Collagen Mimetic Peptide from Triple Helix to Nanofibre and Hydrogel. *Nat. Chem.* **2011**, *3*, 821–828.
38. Matson, J. B.; Newcomb, C. J.; Bitton, R.; Stupp, S. I. Nanostructure-Templated Control of Drug Release from Peptide Amphiphile Nanofiber Gels. *Soft Matter* **2012**, *8*, 3586–3595.

39. Matson, J. B.; Zha, R. H.; Stupp, S. I. Peptide Self-Assembly for Crafting Functional Biological Materials. *Curr. Opin. Solid State Mater. Sci.* **2011**, *15*, 225–235.

40. Soukasene, S.; Toft, D. J.; Moyer, T. J.; Lu, H. M.; Lee, H. K.; Standley, S. M.; Cryns, V. L.; Stupp, S. I. Antitumor Activity of Peptide Amphiphile Nanofiber-Encapsulated Camptothecin. *ACS Nano* **2011**, *5*, 9113–9121.

41. Aluri, S.; Pastuszka, M. K.; Moses, A. S.; MacKay, J. A. Elastin-Like Peptide Amphiphiles Form Nanofibers with Tunable Length. *Biomacromolecules* **2012**, *13*, 2645–2654.

42. Paramonov, S. E.; Jun, H. W.; Hartgerink, J. D. Self-Assembly of Peptide-Amphiphile Nanofibers: The Roles of Hydrogen Bonding and Amphiphilic Packing. *J. Am. Chem. Soc.* **2006**, *128*, 7291–7298.

43. Hsu, L.; Cvetanovich, G. L.; Stupp, S. I. Peptide Amphiphile Nanofibers with Conjugated Polydiacetylene Backbones in Their Core. *J. Am. Chem. Soc.* **2008**, *130*, 3892–3899.

44. Jordan, M. A.; Wilson, L. Microtubules as a Target for Anticancer Drugs. *Nat. Rev. Cancer* **2004**, *4*, 253–265.

45. Hu, C. M. J.; Zhang, L. F. Nanoparticle-Based Combination Therapy toward Overcoming Drug Resistance in Cancer. *Biochem. Pharmacol.* **2012**, *83*, 1104–1111.

46. Musacchio, T.; Laquintana, V.; Latrofa, A.; Trapani, G.; Torchilin, V. P. Peg-Pe Micelles Loaded with Paclitaxel and Surface-Modified by a Pbr-Ligand: Synergistic Anticancer Effect. *Mol. Pharmaceutics* **2009**, *6*, 468–479.

47. Chan, J. M.; Rhee, J. W.; Drum, C. L.; Bronson, R. T.; Golomb, G.; Langer, R.; Farokhzad, O. C. *In Vivo* Prevention of Arterial Restenosis with Paclitaxel-Encapsulated Targeted Lipid-Polymeric Nanoparticles. *Proc. Natl. Acad. Sci. U.S.A.* **2011**, *108*, 19347–19352.

48. Dabholkar, R. D.; Sawant, R. M.; Mongayt, D. A.; Devarajan, P. V.; Torchilin, V. P. Polyethylene Glycol-Phosphatidylethanolamine Conjugate (Peg-Pe)-Based Mixed Micelles: Some Properties, Loading with Paclitaxel, and Modulation of P-Glycoprotein-Mediated Efflux. *Int. J. Pharm.* **2006**, *315*, 148–157.

49. Potineni, A.; Lynn, D. M.; Langer, R.; Amiji, M. M. Poly-(Ethylene Oxide)-Modified Poly(Beta-Amino Ester) Nanoparticles as a pH-Sensitive Biodegradable System for Paclitaxel Delivery. *J. Controlled Release* **2003**, *86*, 223–234.

50. Huh, K. M.; Lee, S. C.; Cho, Y. W.; Lee, J.; Jeong, J. H.; Park, K. Hydrotropic Polymer Micelle System for Delivery of Paclitaxel. *J. Controlled Release* **2005**, *101*, 59–68.

51. Kim, S.; Kim, J. Y.; Huh, K. M.; Acharya, G.; Park, K. Hydrotropic Polymer Micelles Containing Acrylic Acid Moieties for Oral Delivery of Paclitaxel. *J. Controlled Release* **2008**, *132*, 222–229.

52. Poon, Z.; Lee, J. A.; Huang, S. W.; Prevost, R. J.; Hammond, P. T. Highly Stable, Ligand-Clustered “Patchy” Micelle Nanocarriers for Systemic Tumor Targeting. *Nanomed.-Nanotechnol. Biol. Med.* **2011**, *7*, 201–209.

53. Pattekari, P.; Zheng, Z.; Zhang, X.; Levchenko, T.; Torchilin, V.; Lvov, Y. Top-Down and Bottom-up Approaches in Production of Aqueous Nanocolloids of Low Solubility Drug Paclitaxel. *Phys. Chem. Chem. Phys.* **2011**, *13*, 9014–9019.

54. Liu, F.; Park, J. Y.; Zhang, Y.; Conwell, C.; Liu, Y.; Bathula, S. R.; Huang, L. Targeted Cancer Therapy with Novel High Drug-Loading Nanocrystals. *J. Pharm. Sci.* **2010**, *99*, 3542–3551.

55. Chiti, F.; Dobson, C. M. *Annu. Rev. Biochem.* **2006**, *75*, 333–366.

56. Missirlis, D.; Chworus, A.; Fu, C. J.; Khant, H. A.; Krogstad, D. V.; Tirrell, M. Effect of the Peptide Secondary Structure on the Peptide Amphiphile Supramolecular Structure and Interactions. *Langmuir* **2011**, *27*, 6163–6170.

57. Ruzza, P.; Calderan, A.; Guiotto, A.; Osler, A.; Borin, G. Tat Cell-Penetrating Peptide Has the Characteristics of a Poly-(Proline) II Helix in Aqueous Solution and in SDS Micelles. *J. Pept. Sci.* **2004**, *10*, 423–426.

58. Rucker, A. L.; Creamer, T. P. Polyproline II Helical Structure in Protein Unfolded States: Lysine Peptides Revisited. *Protein Sci.* **2002**, *11*, 980–985.

59. Kalaria, D. R.; Sharma, G.; Beniwal, V.; Kumar, M. N. V. R. Design of Biodegradable Nanoparticles for Oral Delivery of Doxorubicin: *In Vivo* Pharmacokinetics and Toxicity Studies in Rats. *Pharm. Res.* **2009**, *26*, 492–501.

60. Mu, L.; Feng, S. S. PLGA/TPGS Nanoparticles for Controlled Release of Paclitaxel: Effects of the Emulsifier and Drug Loading Ratio. *Pharm. Res.* **2003**, *20*, 1864–1872.

61. Lee, B. S.; Park, K.; Park, S.; Kim, G. C.; Kim, H. J.; Lee, S.; Kil, H.; Oh, S. J.; Chi, D. Y.; Kim, K.; et al. Tumor Targeting Efficiency of Bare Nanoparticles Does Not Mean the Efficacy of Loaded Anticancer Drugs: Importance of Radionuclide Imaging for Optimization of Highly Selective Tumor Targeting Polymeric Nanoparticles with or without Drug. *J. Controlled Release* **2010**, *147*, 253–260.

62. Drexhage, K. H. Fluorescence Efficiency of Laser-Dyes. *J. Res. Natl. Bur. Stand. Sect. A* **1976**, *80*, 421–428.

63. Trapani, A.; Sitterberg, J.; Bakowsky, U.; Kissel, T. The Potential of Glycol Chitosan Nanoparticles as Carrier for Low Water Soluble Drugs. *Int. J. Pharm.* **2009**, *375*, 97–106.

64. Diaz, J. F.; Strobe, R.; Engelborghs, Y.; Souto, A. A.; Andreu, J. M. Molecular Recognition of Taxol by Microtubules - Kinetics and Thermodynamics of Binding of Fluorescent Taxol Derivatives to an Exposed Site. *J. Biol. Chem.* **2000**, *275*, 26265–26276.

65. Marcus, A. I.; O’Brate, A. M.; Buey, R. M.; Zhou, J.; Thomas, S.; Khuri, F. R.; Andreu, J. M.; Diaz, F.; Giannakakou, P. Farnesyltransferase Inhibitors Reverse Taxane Resistance. *Cancer Res.* **2006**, *66*, 8838–8846.

66. Lee, J. S.; Feijen, J. Biodegradable Polymersomes as Carriers and Release Systems for Paclitaxel Using Oregon Green (R) 488 Labeled Paclitaxel as a Model Compound. *J. Controlled Release* **2012**, *158*, 312–318.

67. Xu, P. S.; Gullotti, E.; Tong, L.; Highley, C. B.; Errabelli, D. R.; Hasan, T.; Cheng, J. X.; Kohane, D. S.; Yeo, Y. Intracellular Drug Delivery by Poly(Lactic-co-Glycolic Acid) Nanoparticles, Revisited. *Mol. Pharmaceutics* **2009**, *6*, 190–201.

68. Westedt, U.; Kalinowski, M.; Wittmar, M.; Merdan, T.; Unger, F.; Fuchs, J.; Schaller, S.; Bakowsky, U.; Kissel, T. Poly(Vinyl Alcohol)-Graft-Poly(Lactide-co-Glycolide) Nanoparticles for Local Delivery of Paclitaxel for Restenosis Treatment. *J. Controlled Release* **2007**, *119*, 41–51.

69. Boulikas, T.; Tsogas, I. Microtubule-Targeted Antitumor Drugs: Chemistry, Mechanisms and Nanoparticle Formulations. *Gene Ther. Mol. Biol.* **2008**, *12B*, 313–357.

70. Xiong, X. B.; Ma, Z. S.; Lai, R.; Lavasanifar, A. The Therapeutic Response to Multifunctional Polymeric Nano-Conjugates in the Targeted Cellular and Subcellular Delivery of Doxorubicin. *Biomaterials* **2010**, *31*, 757–768.

71. Sai, Y.; Kajita, M.; Tamai, I.; Wakama, J.; Wakamiya, T.; Tsuji, A. Adsorptive-Mediated Endocytosis of a Basic Peptide in Enterocyte-Like Caco-2 Cells. *Am. J. Physiol.* **1998**, *275*, G514–G520.

72. Missirlis, D.; Khant, H.; Tirrell, M. Mechanisms of Peptide Amphiphile Internalization by SJSA-1 Cells *In Vitro*. *Biochemistry* **2009**, *48*, 3304–3314.

73. Chen, H. T.; Kim, S. W.; Li, L.; Wang, S. Y.; Park, K.; Cheng, J. X. Release of Hydrophobic Molecules from Polymer Micelles into Cell Membranes Revealed by Förster Resonance Energy Transfer Imaging. *Proc. Natl. Acad. Sci. U.S.A.* **2008**, *105*, 6596–6601.

74. Riley, R. J.; Martin, I. J.; Cooper, A. E. The Influence of DMPK as an Integrated Partner in Modern Drug Discovery. *Curr. Drug Metab.* **2002**, *3*, 527–550.

75. Conner, S. D.; Schmid, S. L. Regulated Portals of Entry into the Cell. *Nature* **2003**, *422*, 37–44.

76. Silverstein, S. C.; Steinman, R. M.; Cohn, Z. A. Endocytosis. *Annu. Rev. Biochem.* **1977**, *46*, 669–722.

77. Ghose, A. K.; Viswanadhan, V. N.; Wendoloski, J. J. A Knowledge-Based Approach in Designing Combinatorial or Medicinal Chemistry Libraries for Drug Discovery. 1. A Qualitative and Quantitative Characterization of Known Drug Databases. *J. Comb. Chem.* **1999**, *1*, 55–68.

78. Veber, D. F.; Johnson, S. R.; Cheng, H. Y.; Smith, B. R.; Keith, W.; Ward, K. W.; Kopple, K. D. Molecular Properties That Influence the Oral Bioavailability of Drugs. *J. Med. Chem.* **2002**, *45*, 2615–2623.

79. Harush-Frenkel, O.; Rozentur, E.; Benita, S.; Altschuler, Y. Surface Charge of Nanoparticles Determines Their

Endocytic and Transcytotic Pathway in Polarized MDCK Cells. *Biomacromolecules* **2008**, *9*, 435–443.

80. Surapaneni, M. S.; Das, S. K.; Das, N. G. Designing Paclitaxel Drug Delivery Systems Aimed at Improved Patient Outcomes: Current Status and Challenges. *ISRN Pharmacol.* **2012**, *2012*, 623139.

81. Bermudo, M.; Avdeef, A.; Ruiz, A.; Nalda, R.; Ruell, J. A.; Tsinman, O.; Gonzalez, I.; Fernandez, C.; Sanchez, G.; Garrigues, T. M.; *et al.* Pampa - a Drug Absorption *in Vitro* Model 7. Comparing Rat *in Situ*, Caco-2, and Pampa Permeability of Fluoroquinolones. *Eur. J. Pharm. Sci.* **2004**, *21*, 429–441.

82. Leeson, P. D.; Springthorpe, B. The Influence of Drug-Like Concepts on Decision-Making in Medicinal Chemistry. *Nat. Rev. Drug Discovery* **2007**, *6*, 881–890.

83. Benny, O.; Fainaru, O.; Adini, A.; Cassiola, F.; Bazinet, L.; Adini, I.; Pravda, E.; Nahmias, Y.; Koirala, S.; Corfas, G.; *et al.* An Orally Delivered Small-Molecule Formulation with Antiangiogenic and Anticancer Activity. *Nat. Biotechnol.* **2008**, *26*, 799–807.

84. Robinson, R.; Viviano, S. R.; Criscione, J. M.; Williams, C. A.; Jun, L.; Tsai, J. C.; Lavik, E. B. Nanospheres Delivering the Egfr Tki Ag1478 Promote Optic Nerve Regeneration: The Role of Size for Intraocular Drug Delivery. *ACS Nano* **2011**, *5*, 4392–4400.